Journal of Membrane Science 706 (2024) 122942



Contents lists available at ScienceDirect

Journal of Membrane Science

journal homepage: www.elsevier.com/locate/memsci





Tuning the interlayer spacing of graphene oxide membrane *via* surfactant intercalation for ultrafast nanofiltration

Rajakumari Krishnamoorthi [a], Fraz Saeed Butt [a], Nurul A. Mazlan [a], Siyu Chen [a], Norbert Radacsi [a], Shuiqing Yang [b], Yeomin Yoon [c,d], Yi Huang [a,*]

[a] School of Engineering, Institute for Materials & Processes, The University of Edinburgh, Robert Stevenson Road, Edinburgh, EH9 3FB, UK
[b] Jiangsu Dingying New Materials Co., Ltd., Changzhou, Jiangsu, 213031, China
[c] Department of Environmental Science and Engineering, Ewha Womans University, 52 Ewhayeodae-gil, Seodaemun-gu, Seoul, 03760, Republic of Korea
[d] Department of Civil and Environmental Engineering, University of South Carolina, Columbia, 300 Main Street, SC, 29208, USA

ARTICLE INFO

Keywords:
Graphene oxide
Lamellar membrane
Intercalation
Surfactant
Dye separation

ABSTRACT

A facile method has been developed to fabricate lamellar composite graphene oxide (CGO) membranes by incorporating positively charged surfactants – cetyltrimethylammonium bromide (CTAB). The interlayer spacing of GO nanosheets was regulated by the sum of both vertical and horizontal alignment of CTAB on the GO surface *via* electrostatic interaction. The CTAB intercalated GO membrane exhibited an internal layer spacing of 16.97 Å compared to 8.26 Å for the GO membrane. The obtained CGO lamellar membrane with well-defined nanochannels showed ultrafast pure water flux of ~1112 L h^{-1} m^{-2} bar^{-1} and an excellent separation efficiency of >99 % towards negatively charged organic dye molecules at a high permeation flux of ~932 L h^{-1} m^{-2} bar^{-1}, which was nearly 2.5-fold enhancement compared with that of the pristine GO membrane (~400 L h^{-1} m^{-2} bar^{-1}). The electrostatic and π–π interaction forces between the CGO membrane and organic dye molecules played a major role in the overall dye separation mechanism. Furthermore, the CGO membrane demonstrated excellent stability with no loss in separation performance (>96 % organic molecules rejection) after exposure to various pH solutions and deionized water (DI) water. The current work provides a straightforward approach for the formation of highly tunable and stable CTAB-intercalated GO membranes for ultrafast molecular separation.

1. Introduction

Over the past few years, rapid industrialization and population growth have led to a surge in economic activities, producing a substantial amount of wastewater across domestic, industrial, and agricultural sectors. The global freshwater crisis poses a severe threat to the environment and ecosystems [1,2]. Importantly, sectors like textile, paper, leather, and cosmetics are major contributors, producing over 7 × 10^5 tons of dyes annually and these dyes possess complex structures, high chromaticity, toxicity, and a non-degradable structure [3,4]. Unfortunately, around 10–15 % of these dyes are discharged into wastewater, making them a primary source of water pollution [5–8]. In this situation, there is an urgent need to address wastewater dye contamination and promote sustainable practices in these industries that can eliminate organic pollutants at a low cost and in an eco-friendly manner. Among the existing technologies [8–11], membrane-based separation technology, such as ultrafiltration (UF) and nanofiltration (NF), has grown exponentially for removing organic dye contaminants and has become the most favoured technology due to its advantages, including cost-effectiveness, a straightforward operation, and relatively low energy consumption [12–16]. However, these membranes often encounter challenges such as irreversible fouling, the trade-off between solute rejection and water permeability, and the low chemical resistance of traditional polymeric membranes [17]. As a result, new membrane materials that can enhance selectivity, water permeability, and membrane stability are in urgent demand.

In recent years, two-dimensional (2D) materials-based ultrathin membranes have been studied for nanofiltration applications. These materials include metal-organic frameworks (MOFs) [18–20], 2D nanomaterials [21], carbon nitride (g-C_3N_4) [22], MXene [23,24], and covalent organic frameworks (COFs) [25]. Among these 2D materials, graphene oxide (GO) based membranes with lamellar structures have gained great interest as versatile materials in the field of separation technology due to their well-defined nanochannels, molecular sieving

* Corresponding author.
E-mail address: Yi.Huang@ed.ac.uk (Y. Huang).

https://doi.org/10.1016/j.memsci.2024.122942
Received 26 March 2024; Received in revised form 20 May 2024; Accepted 27 May 2024
Available online 28 May 2024
0376-7388/© 2024 The Authors. Published by Elsevier B.V. This is an open access article under the CC BY-NC license (http://creativecommons.org/licenses/by-nc/4.0/).

properties, and chemical and mechanical stability [26–28]. Furthermore, GO can readily react with other substances due to its abundant functional groups, such as epoxide, carboxylic, and hydroxyl groups [29,30]. These groups contribute to its remarkable characteristics, such as hydrophilicity and surface charge, thereby providing abundant chemical reaction sites for further modifications [31–33]. In a lamellar membrane, the flow of permeants follows a tortuous pathway. Initially, they pass through the in-plane gaps and subsequently navigate through nanochannels between the adjacent layers. The arrangement of these nano-channels within the adjacent GO monolayers plays a significant role in determining both separation efficiency and permeance flux [34]. However, the inherent characteristics of GO nanosheets, including their long tortuous routes and tight channel sizes, result in a reduction of permeance. To address these issues, numerous efforts have been made to regulate the nanochannels by adjusting or tuning the adjacent nanosheet layers including chemical modification of GO membranes [35], intercalation of divalent and multivalent metal ions or nanoparticles between GO nanosheets [36–38], chemical cross-linking [39], and reduction of GO [40]. Among these approaches, the intercalation of nano spacers between the adjusted monolayers is widely acknowledged for enhancing permeance flux and separation efficiency [41]. Various materials, such as carbon nanotubes [42], nanoparticles, and organic molecules, have been employed for this purpose. As a consequence, these interventions increase the interlayer spacing, which may inadvertently increase the penetration flux of molecules in the required size range, thereby compromising their efficiency as size-selective membranes. Therefore, it is essential to achieve a high flux while fine-tuning interlayer spacing for targeting high separation efficiency to resolve the trade-off between permeance and rejection.

Aquaporins are a type of biological transmembrane protein that exhibits a hierarchical channel structure characterized by a precisely tuned microchemical environment. They can regulate water movement through cell membranes with exceptional permselectivity for molecules and ions [43–45]. Aquaporin proteins self-assemble into hourglass-shaped channels, featuring a broad hydrophilic region that facilitates high water permeability and a narrow hydrophobic region that promotes ionic rejection [43,46]. Inspired by the unique structure of aquaporin, there has been a growing interest in designing and developing biomimetic membranes with multi-space channels to achieve high permeance flux and effective rejection of contaminants. Several aquaporin-embedded or mimetic polymeric membranes have been reported in the literature [47,48]. Notably, two-dimensional membranes have been explored to a limited extent. For instance, Lee et al. reported the incorporation of aquaporin into graphene oxide-based membranes, demonstrating high water permeance and simultaneous salt rejection [49]. Additionally, a fluffy-like amphiphilic graphene oxide (f-GO) was synthesized by grafting a silane coupling agent (KH570) on graphene oxide sheets, which exhibited excellent antifouling properties [50]. Alternatively, Cetyltrimethylammonium bromide (CTAB) is an important amphiphilic and positively charged surfactant with a long 16-carbon tail and a quaternary ammonium head group. CTAB has been extensively studied as a coating, stabilizing, and structure-directing agent in the synthesis of inorganic materials [51,52]. Moreover, CTAB has been characterized by excellent penetration, flexibility, and antistatic properties [53]. It effectively mitigates the stacking of graphene oxide (GO) and offers a versatile platform for designing functional structures *via* electro-stacking and hydrophobic interactions. Furthermore, CTAB exhibits self-assembled structures like liposomes and multilayers in aqueous solutions.

Herein we report a simple fabrication of GO lamellar composite membrane (CGO) *via* intercalation of a positively charged surfactant cetyltrimethylammonium bromide (CTAB) for nanofiltration applications. Specifically, CGO lamellar membranes were synthesized *via* a reaction between the hydroxyl groups of GO and CTAB head groups ($-^{+}N-CH_3$), and hydrophobic forces between CTAB hydrocarbon tails. We have tuned the interlayer spacing of GO nanosheets by controlling the alignment of CTAB on the GO surface and the CTAB concentration. The as-prepared CGO membrane was used for the removal of organic dye molecules from wastewater, and its permeation flux was also investigated. In addition, the CGO membrane recyclability and stability were also studied under different pH environments.

2. Experimental

2.1. Materials

Graphite flakes (>99.5 %, 325 mesh), sodium nitrate ($NaNO_3$ >99.0 %), potassium permanganate ($KMnO_4$, >99.0 %), reactive black 5 ($C_{26}H_{21}N_5Na_4O_{19}S_6$, M. wt.: 991.82 g mol^{-1}), direct red 80 ($C_{45}H_{26}N_{10}Na_6O_{21}S_6$, M. wt.: 1373.07 g mol^{-1}), H_2O_2 (30 % in H_2O), and hydrochloric acid (HCl, 37 %) were purchased from Sigma Aldrich. Methylene blue ($C_8H_{11}ClN_3S$, M. wt.: 319.85 g mol^{-1}), methyl orange ($C_{14}H_{14}N_3NaO_3S$, M. wt.: 327.33 g mol^{-1}), rhodamine B ($C_{28}H_{31}ClN_2O_3$, M. wt.: 479.02 g mol^{-1}), rose bengal ($C_{20}H_4Cl_4I_4O_5$, M. wt.:373.07 g mol^{-1}), and uni-blue A ($C_{22}H_{16}N_2O_7S_2$, M. wt.: 506.48 g mol^{-1}), was obtained from Alfa Aesar. Sulphuric acid (H_2SO_4, 97 %) was purchased from Honeywell. A nylon membrane (47 mm diameter, 0.2 μm pore size) was ordered from Whatman, Inc. All chemicals were used without further purification. Deionized water (18.2 M Ω-cm) was obtained from a Milli-Q water purification system.

2.2. Characterizations

The concentration of single-layered graphene oxide (SLGO) solution was obtained from Thermo Scientific Evolution 60 UV–Vis's spectrophotometer (UV–Vis spectra) and the thickness of the SLGO nanosheet was estimated with the Atomic force microscopy (AFM) images obtained from a Multimode Nanoscope V system (Veeco, Santa Barbara, CA) operating in tapping mode. The surface and cross-sectional morphology of the prepared membrane were characterized using a JEOL JSM-IT100 scanning electron microscope (SEM). Elemental mapping of the membrane was performed with Energy-dispersive X-ray (EDX) analysis using an Oxford Instruments X-maxN 150 detector. The water contact angle (WCA) of the membranes was measured with the Ossila contact angle goniometer. For binding energy, a Scienta 300 analyzer with SPECS monochromatic XPS equipped with Al Kα radiation was used. To look into the material crystallinity and the *d* spacing between the GO layers of the membrane was calculated X-ray diffraction (XRD; Bruker D8 Advance) analysis was carried out with Cu Kα radiation in a 2θ range of 4.0°–55.0°. The local molecular structure of the membranes was investigated by Fourier Transform Infrared Spectroscopy (FTIR; Nicolet iS10) with a range of 500–4000 cm^{-1}. The molecular structure and defective surface of the membrane were analyzed by Raman spectroscopy using a 20 × objective lens (JASCO NRS-5100 series). UV–Vis spectra were obtained to analyze the dye concentrations using a Thermo Scientific Evolution 60 UV–Vis spectrophotometer.

2.3. Synthesis of graphene oxide

The synthesis of graphene oxide was carried out using a previously reported recipe [53]. Briefly, 1 g of P_2O_5 and 3 g of $KMnO_4$ were mixed with 23 mL of concentrated H_2SO_4 for 3 minutes (min). Subsequently, a mixture consisting of 1g of graphite flakes (Alfa Aesar, 325 mesh) and 0.5 g of $NaNO_3$ were ground together and added to the reaction mixture for 10 min. The reaction mixture was then gently heated from room temperature (25 °C) to 35 °C under stirring for 1 h, and 10 mL of DI water was carefully added dropwise to prevent overheating from the exothermic reaction. The temperature of the reaction was then raised to 85 °C and maintained for 15 min. Afterwards, the resultant reaction mixture was cooled to room temperature, and 10 mL of H_2O_2 was added. The synthesized GO slurry was collected in yellow color and washed and filtered several times with aqueous HCl solution (35 % HCl: H_2O = 10

mL :100 mL). This was followed by dialysis in DI water until the solution reached a neutral pH (~7.0). Finally, the samples were collected and freeze-dried for further use.

2.4. Preparation of SLGO

0.3 g of the above-collected GO powder was carefully dispersed in 30 ml of deionized (DI) water using vortex mixing at 2400 rpm for 3 min, followed by 2 h of sonication. Subsequently, the GO dispersion solution underwent centrifugation at 8000 rpm for 1 h at 20 °C to eliminate multilayer graphite flakes and impurities. The resulting supernatant was carefully collected and stored as the stock solution of single-layer graphene oxide (SLGO). The concentration of the prepared SLGO was determined with the UV–Vis spectrometer, while the dimensions and thickness of SLGO nanosheets were analyzed using AFM (Fig. S1).

2.5. Fabrication of single-layer graphene oxide membranes

The non-intercalated single-layer graphene oxide membrane (NGO) was fabricated by coating the SLGO nanosheets directly on the nylon membrane support (pore size = 200 nm) by vacuum filtration technique (Millipore filtration system). The GO layer thickness was controlled by calculating the amount of GO (0.01 mg mL^{-1}) in the SLGO suspension according to the following equation (1), [54].

$$m = \rho V = \rho Sh \quad (1)$$

Where 'm' is the amount of GO in the SLGO suspension, 'ρ' is the density of GO (ρ ~ 2.1 g cm^{-3}), 'S' is the effective filtration area, and 'h' is the desired thickness of the GO layer.

2.6. Fabrication of CTAB and GO-modified (CGO) nylon membranes

The GO and CTAB intercalated membranes were prepared using the vacuum filtration technique. Specifically, the above-prepared SLGO solution (0.01 mg mL^{-1}) was mixed with various concentrations of CTAB surfactant (10, 20, 30, and 50 mg) in 200 mL of DI water using a vortex mixer for 2 min, followed by 1 h of Sonication. The resultant mixture was subsequently filtered through a nylon membrane support (pore size = 200 nm) *via* vacuum filtration (Millipore filtration system). Finally, the as-prepared membrane was subjected to heat treatment at 80 °C for 12 h to enhance the interaction between the GO-CTAB. The obtained product was named CGO-*x*, where '*x*' represents the amount of surfactant (mg) used, as indicated in Table 1.

The interlayer spacing of Pristine Graphene oxide and CGO lamellar membrane has been calculated by the following equation [55].

$$d = \frac{n\lambda}{2\sin(\theta)} \quad (2)$$

Whereas, '*n*' is the order of diffraction, 'λ' is the wavelength of the X-ray used, d is the spacing between the crystal lattice planes and '*θ*' is the angle of diffraction. The calculated *d*-spacing of the membrane were presented in Table S1.

Table 1
Composition of prepared CGO membranes.

Sample	Conc. of GO (mg ml^{-1})	Amount of CTAB (*x*) (mg)	Volume of total solution (ml)
p-Nyl	–	–	–
NGO	0.01	0	200
CGO-10	0.01	10	200
CGO-20	0.01	20	200
CGO-30	0.01	30	200
CGO-50	0.01	50	200

2.7. Membrane separation performance

The filtration performance of the membrane was assessed using a millipore vacuum filtration set-up at a pressure of 0.5 bar. The permeance flux 'F' of the membrane was determined by calculating the volume of permeate in unit time using equation (2) [56].

$$F = V / (A \times \Delta T \times \Delta P) \quad (3)$$

Where 'V' is the volume of permeate in litres (L), 'A' is the effective filtration area in m^2, 'Δt' is the filtration time in h, and 'ΔP' is the applied pressure. The separation efficiency (R) was calculated using the following equation (3) [56].

$$R(\%) = \frac{(C_f - C_p) \times V}{C_f} \times 100 \quad (4)$$

Where 'C_P' and 'C_F' are the dye concentrations (ppm) in the permeate and the feed solution, respectively.

2.8. Adsorption capacity of the CGO membranes

Seven different dyes, including direct red (DR-80), rhodamine B (Rh-B), rose-bengal (RB), reactive black (RB-5), uni-blue A (UB-A), methyl orange (MO), and methylene blue (MB), were used to study the adsorption capacity of the as-prepared CGO membranes. The membranes were cut into 10 mm diameter to ensure the same surface area for each sample. The Adsorption experiment was performed by immersing the membrane sample into a 25 mL dye solution with a concentration of 50 mg mL^{-1} for 24 h. The concentration of dye solution before and after the adsorption was analyzed using UV–visible spectra. The amount of dye adsorbed was calculated using the following equation (4) [54].

$$Q = \frac{(C_o - C_t) \times V}{A} \quad (4)$$

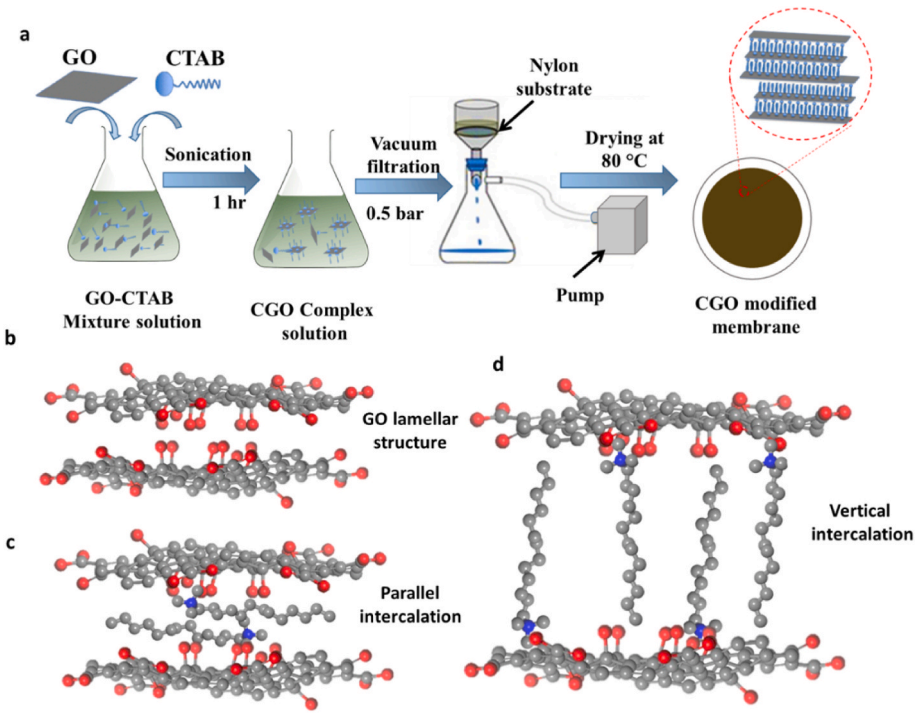
Where, 'C_o' (mg mL^{-1}) is the initial dye concentration in the feed solution in mg mL^{-1}, and 'C_t' is the dye concentration in the solution after adsorption in mg L^{-1}. 'V' is the solution volume in litres (L), 'A' is the effective surface area for adsorption in m^2.

3. Results and discussion

3.1. Fabrication and characterization of CGO-modified membranes

The procedure for CGO membrane fabrication is illustrated in Scheme 1a. Initially, an aqueous solution containing single-layer graphene Oxide (SLGO) and cetyltrimethylammonium bromide (CTAB) was mixed vigorously to achieve a uniform solution. Subsequently, the mixture was subjected to 1 h of sonication to form micelles composed of GO and CTAB, resulting from the electrostatic interaction between the GO and CTAB head groups. The resulting mixture was then deposited onto a nylon membrane, thus forming the CTAB-intercalated GO membrane (CGO). To further enhance the interaction between the quaternary ammonium group ($^{+}N–CH_4$) of CTAB and the carboxyl and hydroxyl groups of GO, the membrane was subjected to a heating process. The molecular structure and the possible intercalation of CTAB between the GO layers are presented in Scheme 1b to 1d. The images for both the prepared NGO and CGO membranes are presented in Figs. S2a and S2b.

The as-prepared membrane was characterized using FTIR (Fig. 1a and b). The pristine nylon membrane substrate (P-Nyl) showed typical absorption bands at 3296 cm^{-1}, 1637 cm^{-1}, and 1542 cm^{-1} corresponding to the stretching vibrations of N–H bonds and C=O groups and bending vibration of N–H groups, respectively [57]. The GO powder and the SLGO-modified nylon membrane (NGO) displayed characteristic



Scheme 1. (a) Schematic representation of CGO membrane fabrication using vacuum filtration set-up and (b)–(c) possible intercalation and arrangement of (b) GO lamellar membrane, (c) GGO lamellar membrane with parallel intercalation, and (d) GGO lamellar membrane with vertical intercalation.

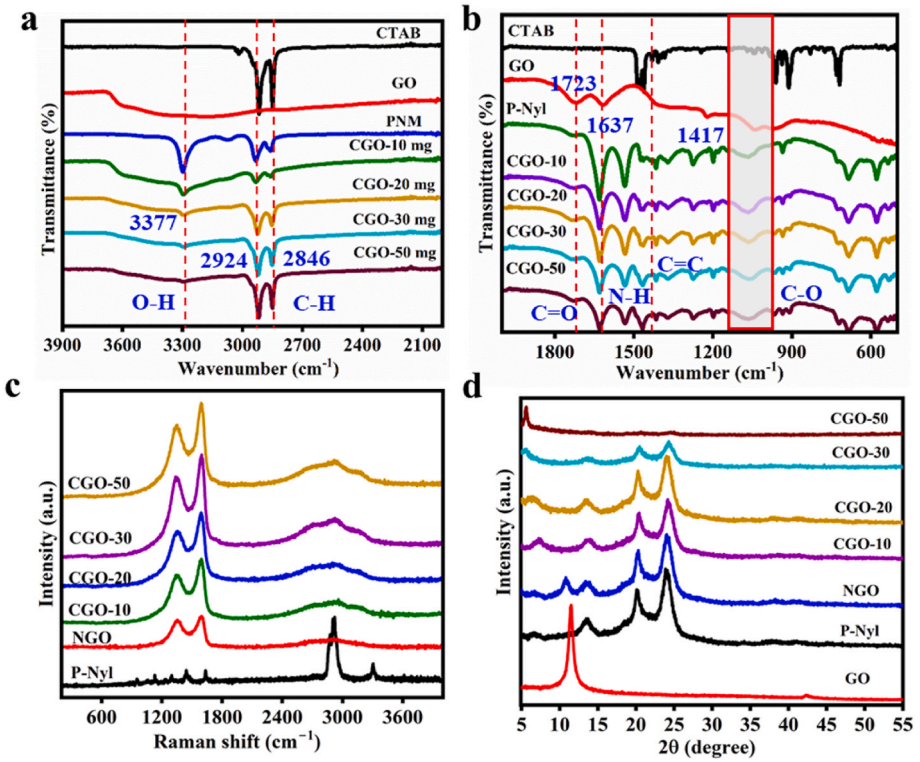


Fig. 1. (a) and (b) FTIR, (c) Raman and (d) XRD spectra of P-Nyl, NGO and CGO-10, CGO-20, CGO-30, and CGO-50 membranes, respectively.

peaks at 1723 cm^{-1}, 1633 cm^{-1}, 1074 cm^{-1}, 1417 cm^{-1}, and 3377 cm^{-1}, which attributed to the presence of carboxyl (–COOH), benzene C=C, epoxy (–O–C–O), and hydroxyl (–OH), respectively [58]. The appearance of absorption bands at 2924 cm^{-1} and 2846 cm^{-1} for the CGO lamellar membrane can be attributed to the stretching vibration of CH_2 and symmetric deformation modes of CH_3–N^+ of the CTAB head group CH_3–N^+, respectively. Notably, these peaks persisted after ethanol washing, confirming the strong attachment of CTAB groups to the GO surfaces. Furthermore, the intensity of the CH_2 and ^+N–CH_3 peaks gradually increased from the membrane sample CGO-10 to CGO-50, confirming the enhanced intercalation of CTAB between the GO layers [59].

Fig. 1c shows the Raman spectra of P-Nyl, NGO, and CGO membranes. In both NGO and CGO samples, the typical peaks 1329 cm^{-1} and 1577 cm^{-1} corresponded to the D band and G band of GO, respectively. The presence of the G band arising from the in-plane vibration of C sp^2 and D band indicates defects and a disordered structure of the graphitic domain. Generally, the intensity ratio of the D band to the G band (I_D/I_G) is used to assess the crystallinity and defect density of the carbon-based material. In this study, the I_D/I_G ratio of the NGO was found to be 0.81 and it increased progressively to 0.82, 0.85, 0.87, and 0.90, for the samples CGO-10, CGO-20, CGO-30, and CGO-50, respectively (Table S2) [60,61]. These results indicate that the CGO sample has a higher degree of disorder and structural defects as compared to the NGO membrane, which primarily originates from the intercalation of CTAB between the GO layers. Interestingly, among all the samples CGO-50 exhibited the highest I_D/I_G ratio, proving an increased interlayer spacing between the GO sheets.

The XRD pattern (Fig. 1d) revealed distinctive characteristics of the membrane samples. For instance, P-Nyl showed characteristic peaks at 20.40° and 23.91°, which corresponds to the (200) and (002/202) planes of crystal forms α1 and α2, respectively. In contrast, the pure GO-coated NGO membrane showed a typical peak at 10.9°, corresponding to the plane 001. Additionally, the interlayer spacing of the NGO membrane was calculated as 8.26 Å, which is comparable with the interlayer spacing reported previously [61,62]. Importantly, upon modification with CTAB, the diffraction peaks were shifted to a lower angle for samples CGO-10 to CGO-50 as the concentration of CTAB content increased (Table S1). Notably, CGO-50 displayed a sharp peak at 5.3°, indicating a significantly expanded interlayer spacing of 16. 64 Å, in comparison to 8.26 Å for NGO [59]. This shift in the XRD peak intensities for the CGO-*x* membranes indicated the presence of various interaction forces such as Van der Waal's forces, electrostatic interactions, and hydrogen bonding, which resulted in the parallel, vertical, or staggered type of CTAB-in-GO intercalations [62,63]. Therefore, the alignment of CTAB to intercalate GO layers was most likely a combination of parallel and vertical intercalation, with vertical intercalation being the main factor for the larger interlayer spacing of the CGO-50.

Fig. 2 shows the surface morphology of P-Nyl, NGO, and CGO membranes. P-Nyl exhibited a highly porous structure and a smooth surface (Fig. 2a). Fig. 2b displayed the formation of a dense and wrinkled GO layer on the surface of the porous P-Nyl substrate (NGO). After the Intercalation of CTAB, CGO membranes (Fig. 2c to f) exhibited a well-preserved layered structure with an increased surface roughness for the sample CGO-10 to CGO-50. The intercalation of CTAB hardly changed the laminated structure of the CGO membrane. Notably, the CGO-50 membranes exhibited an increased thickness of 1.22 μm compared to the 0.4 μm of the NGO membrane (Fig. 3 and S3). Therefore, it is evident that the ordered multilayer structures occurred due to the driving force of molecular interaction between the CTAB and GO self-assembly. The interaction primarily involves the hydrophobic forces of CTAB hydrocarbon tails and the electrostatic attractions between GO and CTAB head groups which was also proved by FT-IR, Raman, and XRD spectra. Moreover, the surface elemental mapping, especially for nitrogen, suggested a uniform distribution of CTAB across the GO layers, as noticed for CGO-50 (Fig. S4).

The XPS was used to investigate the chemical composition of the CGO composite membrane, as shown in Fig. 4a. In the P-Nyl and NGO membranes, the major elements such as carbon, oxygen, and nitrogen were mainly focused. The NGO membrane exhibited a lowered intensity of N1s compared to the P-Nyl due to dense and uniform coverage of GO. Interestingly the N1s peaks exhibited an increase in intensity for CGO-10 and CGO-50 membranes as compared to NGO. This increase was ascribed to the presence of quaternary amino groups from CTAB. In addition, the high-resolution C1s spectra of P-Nyl, NGO, and CGO-50 are shown in Fig. 4b to d, respectively. In the P-Nyl membrane, three distinct peaks at 284.8 eV, 286.4 eV, and 288.1 eV were observed, corresponding to the C–C, C–N, and O=C/O=C–OH groups, respectively. In contrast, the NGO membrane exhibited five new peaks at 284.85 eV, 286.85 eV, 287.29 eV, 288.41 eV, and 290. 01 eV corresponds to the C–C/C=C, C–O, C=O, O–C=O, π–π, and with decreased intensity of C–N at 286.4 eV when compared to P-Nyl, respectively. Moreover, the CGO-50 exhibited five peaks 284.85 eV, 286.08 eV, 286.80 eV, 287.80 eV, and 289.10 eV corresponding to the C–C, C–N, C–O, C=O, and O–C=O, respectively. Interestingly the peak intensity of C–N was increased while C–O intensity was lowered from the NGO substrate. These results prove the successful intercalation of CTAB and suggest that the CGO composite is composed of the CTAB head group and GO with no hydrophobic adsorption occurring between GO and CTAB [64].

Surface topological features of the CGO lamellar membrane were analyzed using an AFM instrument (Fig. 5). The quantitative information regarding surface topography was assessed through the root mean

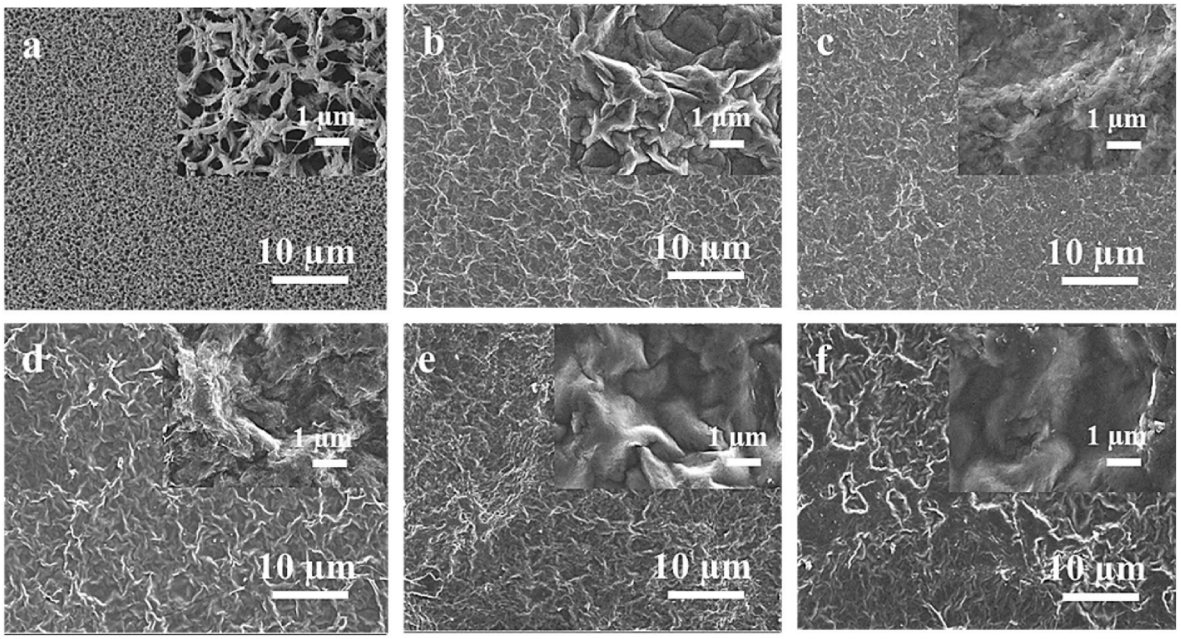


Fig. 2. SEM images of pristine and CGO-modified membranes; (a) P-Nyl, (b) NGO, (c) CGO-10, (d) CGO-20, (e) CGO-30, and (f) CGO-50 membranes, respectively.

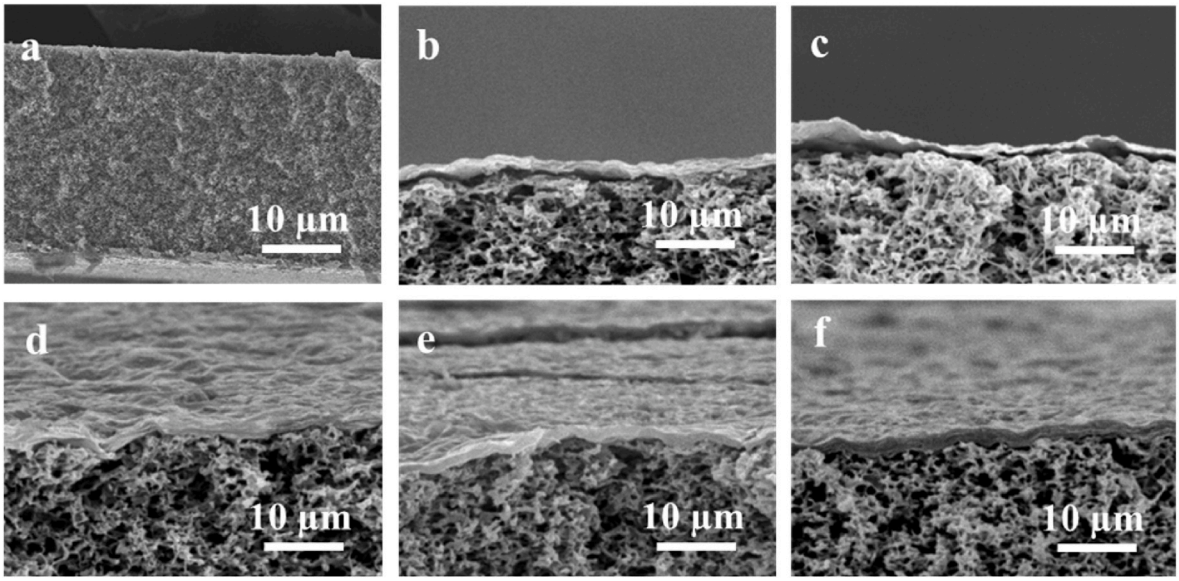


Fig. 3. The SEM cross-sectional images of (a) P-Nyl, (b) NGO, (c) CGO-10, (d) CGO-20, (e) CGO-30, (f) CGO-50 membranes.

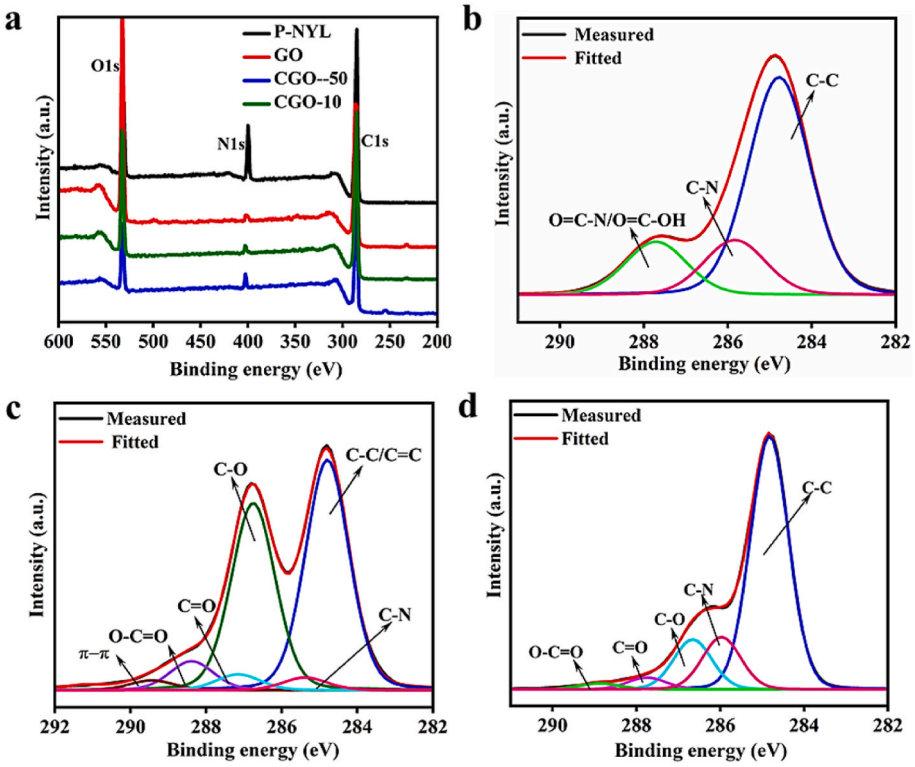


Fig. 4. XPS spectra of Pristine and CGO-modified membranes; (a) full survey spectrum of P-Nyl, NGO, CGO-10, and CGO-50. Peak-fitted high-resolution C1s spectra of (b) P-Nyl, (c) NGO, and (d) CGO-50 membranes.

square (R_q) roughness [65,66]. The obtained results revealed that the P-Nyl membrane exhibited an R_q of 229.8 ± 4 nm with a highly porous structure. After GO coating to form the NGO membrane, the surface roughness drastically decreased to 80.4 ± 12.8 nm. This reduction was attributed to the uniform coverage and wrinkled structure resulting from the even coating of GO. The introduction of CTAB into the GO membrane led to a slight increase in surface roughness. The calculated roughness values were 91.6 ± 21 nm for CGO-10 and 121.3 ± 35 nm for CGO-50. It's worth noting that the higher concentration of CTAB intercalation corresponded to a higher surface roughness. This increase may be attributed to a more porous structure resulting from CTAB intercalation, which, in turn, expanded the interlayer spacing of the CGO membrane, which is also proved by the cross-sectional SEM (Fig. 3 and S3).

3.2. Membrane hydrophilicity and permeability

Wettability is one of the crucial parameters for assessing membrane filtration performance. In this study, the dynamic water contact angle (WCA) was measured to look into membrane wettability (Fig. 6a). The P-

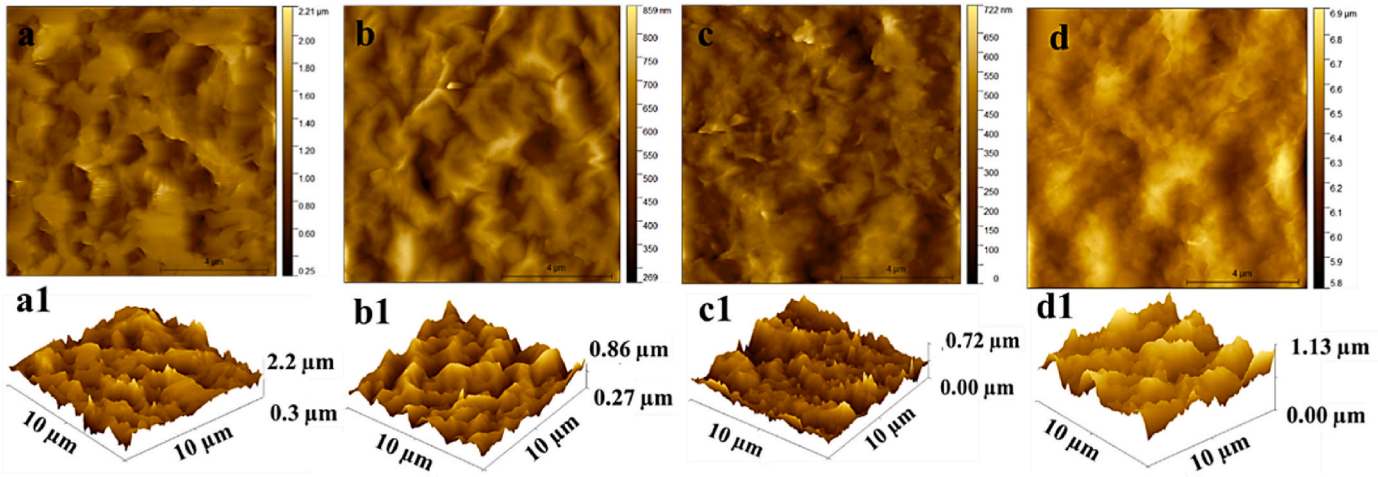


Fig. 5. AFM images and their corresponding 2D images of P-Nyl and CGO modified membranes; (a and a1) P-Nyl, (b and b1) NGO, (c and c1) CGO-10, and (d and d1) CGO-50 membranes.

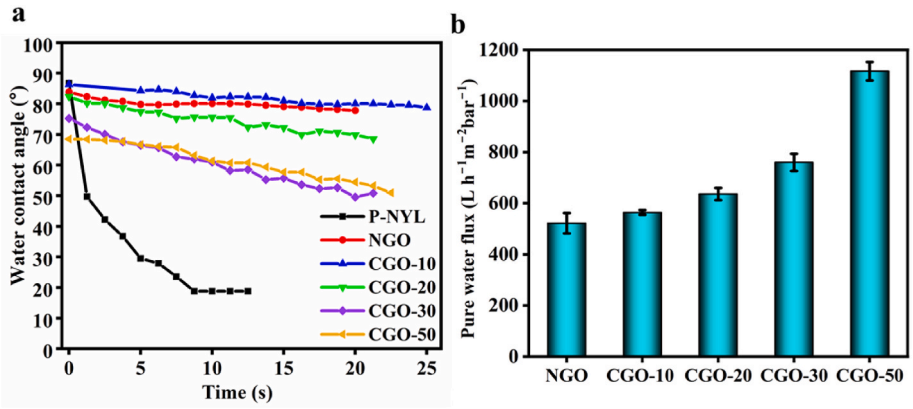


Fig. 6. (a) Dynamics water contact angle and (b) pure water flux of P-Nyl, NGO, CGO-10, CGO-20, CGO-30, and CGO-50 membranes, respectively.

Nyl membrane exhibited an initial WCA of 88 ± 4° and the water droplets fully covered the substrate surface within ~10 s due to the rapid permeation of water through the membrane pores. After coating with GO, the WCA for the NGO membrane was slightly decreased to 75 ± 2°, resulting from the hydrophilic nature of GO due to the abundance of surface functionalities such as hydroxyl, carboxyl and epoxy groups. The WCA values for the NGO membrane did not show any change with time (up to 20 s), suggesting the uniform deposition of GO and reduced pore size of the NGO membrane. Interestingly, the WCA of the CGO membrane showed a further reduction in value upon an increase in the CTAB content. For instance, the CGO-50 exhibited a lower WCA of 51 ± 1°. This is because of the amphiphilic nature of intercalated CTAB between the adjacent GO nanosheets and the formation of enlarged nanochannels, which greatly promote the spreading and permeation of water. The pure water flux properties of the prepared membranes were assessed by passing pure water through the membrane samples under an external pressure of 0.5 bar. The GO-coated NGO membrane exhibited a pure water flux of 522 ± 25 L h^{-1} m^{-2} bar^{-1} (Fig. 6b). However, after CTAB modification the water flux values increased with increasing the CTAB content of the CGO membrane with CGO-10, CGO-20, CGO-30, and CGO-50 exhibiting a water flux equivalent to 563 ± 84 L h^{-1} m^{-2} bar^{-1}, 636 ± 24 L h^{-1} m^{-2} bar^{-1}, 760 ± 13 L h^{-1} m^{-2} bar^{-1}, and 1116 ± 53 L h^{-1} m^{-2} bar^{-1}, respectively. Notably, CGO-50 displayed enhanced water flux due to the increased internal layer spacing of CGO as the result of excessive CTAB intercalation. These results suggested that the CGO membrane exhibited less torturous and more porous nanochannels compared to the NGO membrane, and intercalation of CTAB between the GO improved the water flux by increasing the interlayer spacing and nanochannel formation within the GO nanosheets [66].

3.3. Dye rejection performance

To certify the above results, direct red-80 (DR-80, M. wt., 1373.07 da) dye was used to investigate the separation and rejection performance of all the prepared membranes under 0.5 bar vacuum pressure. For instance, the DR-80 dye permeance and rejection performance of the NGO, CGO-10, CGO-20, CGO-30, and CGO-50, are summarized and compared in Fig. 7a. The concentration of DR-80 in feed and permeate was determined by UV–Vis's spectroscopy (Fig. 7). The corresponding DR-80 molecular structure and photography of the feed and permeate of the respective DR-80 solutions are presented in Fig. 7c and d. The permeance of the P-Nyl membrane exhibited 416 ± 7 L h^{-1} m^{-2} bar^{-1} with a DR-80 rejection of ~60 %. In comparison to widely reported GO lamellar membranes, the water flux and dye rejection of pristine GO in this work are significantly higher, owing to its well-assembled and unique interlayer structure. Specifically, functionalized patches (−OH, −COOH, C−O−C) on neighbouring GO layers facing each other and pristine graphene patches on adjacent GO layers form well-assembled nanostructures. These hydrophilic groups reduce water accumulation sites on the SLGO layers, thereby establishing rapid water transport channels [66–69]. In contrast, the water permeance greatly enhanced

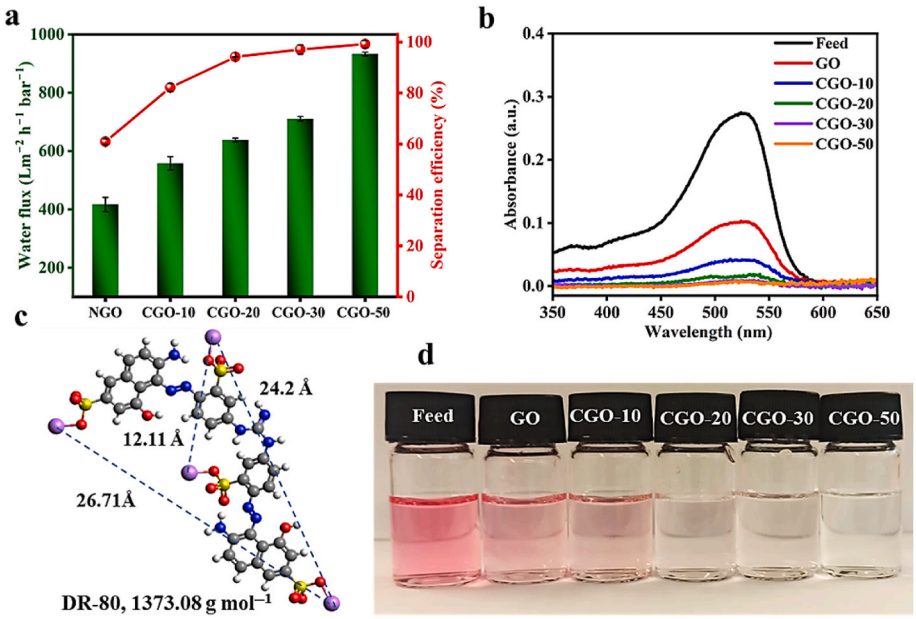


Fig. 7. (a) Direct red-80 (DR-80) dye separation efficiency and water flux of P-Nyl, NGO, CGO-10, CGO-20, CGO-30, and CGO-50, respectively; (b) their corresponding UV visible spectrum; (c) molecular properties of DR-80; and (d) photographic images of dye solution of before and after separation DR-80 dye solution. (For interpretation of the references to color in this figure legend, the reader is referred to the Web version of this article.)

for the CTAB intercalated CGO membrane to ~558 ± 3 L h^{-1} m^{-2} bar^{-1}, ~637 ± 7 L h^{-1} m^{-2} bar^{-1}, ~710 ± 2 L h^{-1} m^{-2} bar^{-1} and ~932 ± 7 L h^{-1} m^{-2} bar^{-1} with the satisfactory rejection of DR-80 equivalent to 82.11 %, 94.1 %, 97.08 %, and 99.18 % for NGO, CGO-10, CGO-20, CGO-30, and CGO-50, respectively. The permeation flux and rejection performance of the CGO membrane increased with an increase in the CTAB content in the GO membrane. Notably, the CGO-50 membranes exhibited a high water flux with an excellent dye rejection efficiency, which is over 65 times higher than that of most commercially used NF membranes [70–72]. This significant enhancement in the membrane performance can be attributed to the increased CTAB intercalation, which resulted in the broadening of GO interlayer spacing, and led to a higher permeation flux. In addition, when increasing the amount of CTAB on the surface, also the increased presence of cationic head groups on the GO surface promotes electrostatic interactions between the dye and CGO membrane, thereby enhancing separation efficiency. This phenomenon resembles the functionality of aquaporin protein [71,72]. Where a reactive surface with more cationic groups effectively rejects dyes, while the increased interlayer spacing facilitates greater water flux. Furthermore, it is worth noting that the molecular size of DR-80 is 26.71 × 24.2 Å (Fig. 7c), which is bigger than the interlayer spacing of CGO (16.97 Å), resulting in increased separation performance. This suggested that the size exclusion played a key role in influencing the separation performance. It is worth noting that only increasing the CTAB amount enhances the nanofiltration performance, so we investigate further increasing the CTAB content higher concentration. Increasing the CTAB content led to an expansion in the interlayer spacing of the GO layers. This was confirmed by XRD analysis (Fig. S6a), which showed that the optimized interlayer spacing was achieved for CGO-50, measuring at ~16.9 Å. Further increments in CTAB content did not result in any significant changes in the interlayer spacing and the filtration performance was also not affected much with CTAB content over 50 mg. Therefore. The CGO 50 was selected as the optimized membrane for further experiments. More explanation can be found in SI (Fig. S6).

To gain a more systematic understanding of the separation mechanism of the CGO composite membrane, we investigated the separation performance for organic dyes with various molecular sizes and different charge properties including rose bengal (RB), methylene blue (MB), methyl orange (MO), rhodamine B (Rh-B), reactive black 5 (RB-5), and uni-blue A (UA). Fig. S5 showed the UV–visible spectra of the corresponding feed and permeate solutions of the used organic dyes, along with their photographic images before and after filtration.

The molecular structures (Fig. 8a) and different charge properties of the tested dyes are presented in Table S3. As shown in Fig. 8b and c separation performance of the CGO-50 exhibited a constant permeance flux of >932 ± 79 L h^{-1} m^{-2} bar^{-1} for all the organic dyes, but with variable rejection rates. For instance, the CGO-50 membranes exhibited higher separation efficiency of 99.18 %, 98.98 %, 98.91 % and 97.8 % for the negatively charged dyes with larger molecular weight, i.e., DR-80 (1373.08 Da), RB (1017.64 Da), RB-5 (991.82 Da), and UB-A (506.48 Da). Another reason for the high removal rate can also be attributed to the negative charge of the dye, which led to the molecules being readily attracted by the positively charged CGO membrane through electrostatic interactions. Consequently, nanochannels of CGO may be partially blocked, resulting in lower rejection efficiency of cationic dyes such as 62.67 % and 59.2 % for MB (319.85 Da, 14.1 × 4.97 Å) and Rh-B (479.02 Da, 16.4527 × 8.27 Å), having sizes smaller than the internal layer spacing of CGO membrane. In contrast, the CGO-50 membrane showed a lower separation efficiency of 50.01 % for MO (327.33 Da, 15.27 × 4.97 Å), which is a lower molecular cut-off than the CGO lamellar structure and bears a negative charge. These results suggest that the separation performance of the membrane is determined by both the principle of size exclusion and electrostatic adsorption [73].

Further, the adsorption performance of the CGO membrane towards different organic dyes used was also investigated to gain further insight into the membrane separation performance and the interaction between the dye molecules and the CGO membrane. As shown in Fig. S7, the CGO-50 membrane exhibited adsorption capacities of 938 ± 91 mg m^{-2}, 1021 ± 15 mg m^{-2}, 1455 ± 10 mg m^{-2}, 805 ± 70 mg m^{-2}, 845 ± 30 mg m^{-2}, 157 ± 10 mg m^{-2}, and 113 ± 20 mg m^{-2} for organic dyes, including DR-80, RB, MO, RB-5, UB-A, Rh-B, and MB, respectively. Interestingly, these results suggested that all the negatively charged organic dyes exhibited high adsorption capacity, with MO showing relatively higher adsorption (1455 ± 10 mg m^{-2}), and low adsorption capacity for positively charged dyes such as Rh-B and MB. This can be attributed to the presence of more cationic head ($^{+}$N–CH$_3$) groups on the surface of the CGO membrane, thus facilitating electrostatic interaction

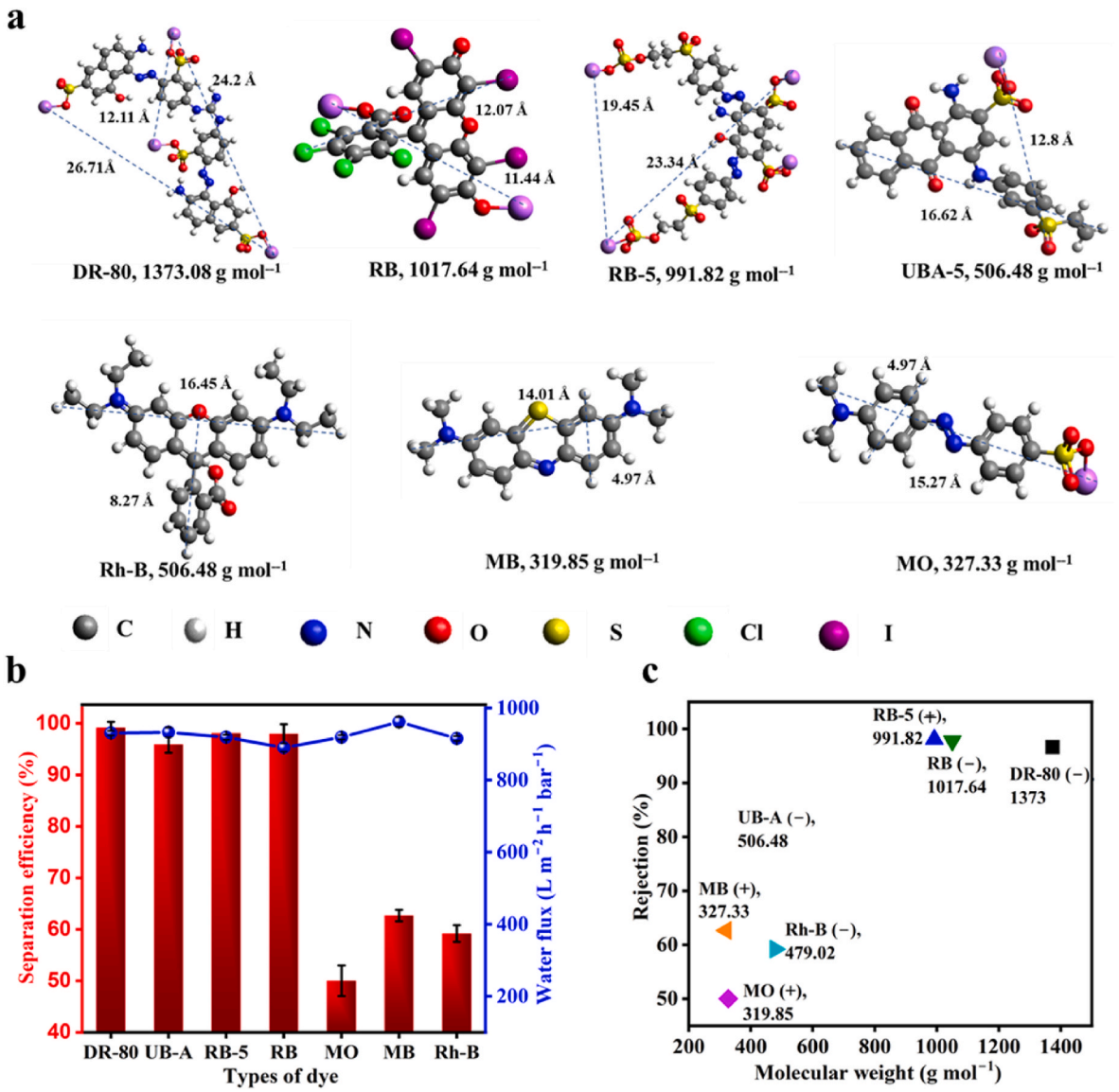


Fig. 8. (a) Molecular properties of different dyes tested in this work (molecular sizes were obtained using the Avogadro software), (b) separation performance of the CGO membrane for various types of dyes, and (c) rejection of different dyes as a function of molecular weight.

between sulfonate groups of the MO and CGO membrane, and also hydrogen bonding and π–π interaction between of MO with GO on the CGO membrane surface, as illustrated in Fig. 9a and b. The above-discussed results confirmed the dye rejection mechanism to be mainly influenced not only by the electrostatic interactions and adsorption of organic dyes on the CGO membrane surface but also by the size and shape selectivity of the well-structured CGO lamellar arrangement (Fig. 9a and b).

3.4. Stability of the membranes

In addition to separation efficiency and water flux, the chemical stability and recyclability of the membrane are critical factors for ensuring long-term separation efficiency in practical applications. The chemical stability of the CGO membrane was assessed by immersing CGO-50 in different pH solutions for 24 h, including pH 4, pH 5, pH 6, pH 7, pH 8, and pH 9. After drying, the morphological changes on the membrane surface were studied using SEM (Fig. S8). As depicted in Fig. S8, following exposure to various pH environments, the CGO membrane morphology remained largely unchanged and retained its original wrinkled structure, confirming its robust chemical stability. This result prompted us to evaluate the separation performance of the CGO membrane after treatment under different pH environments and evaluate its cyclic separation performance. The results showed that permeation flux and rejection performance remained unchanged indicating that the CGO membrane possesses good integrity even under harsh conditions (Fig. 10a). Furthermore, the recycling performance of the CGO-50 membrane was assessed using a freshly prepared CGO-50 membrane. As illustrated in Fig. 10b, through each separation cycle, the separation efficiency consistently exceeded 96 %, maintaining an initial permeation flux of ~924.56 L h^{-1} m^{-2} bar^{-1}.

Furthermore, the effect of cyclic separation tests on membrane stability and surface morphology was further studied using SEM. As shown in Fig. 11a, no significant changes were observed on the surface of the CGO membrane when compared to its original samples (Figs. 2 and 3). Importantly, the membrane retained its wrinkled structure with only a slight reduction in membrane thickness from 1.21 μm to 1.01 μm (Fig. 11b), confirming its stability and consistent dye separation performance. Additionally, the chemical composition was confirmed by XPS C1s fitting spectra, as shown in Fig. 11c. The CGO-50 sample exhibited five peaks even after the five-cycle dye separation test. i.e., 284.85 eV, 286.08 eV, 286.80 eV, 287.80 eV and 289.10 eV,

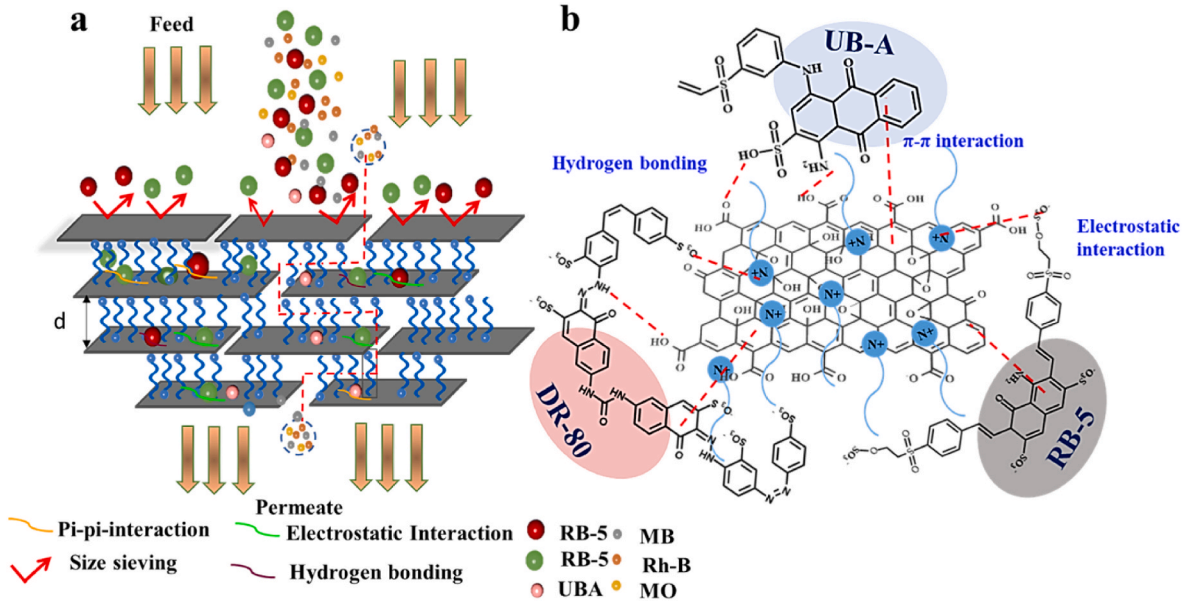


Fig. 9. Schematic illustration of (a) the separation mechanism of CGO membrane and (b) the interaction between organic dyes and CGO surface.

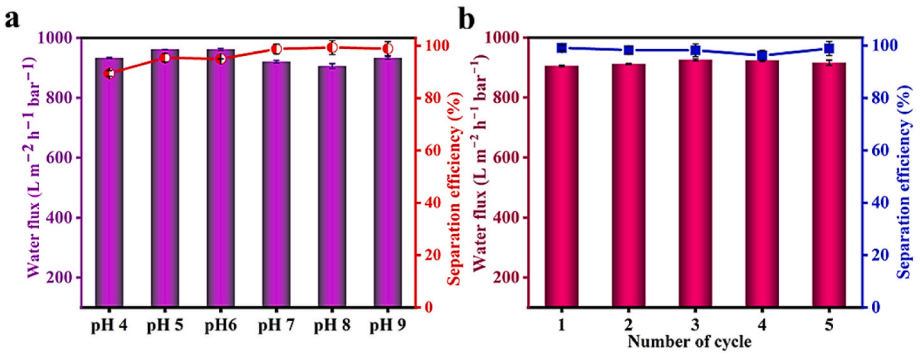


Fig. 10. (a) Separation performance of CGO membrane after soaking for 24 h under various pH solutions and DI water and (b) recycle test of the CGO membrane for 5 cycles.

corresponding to C–C, C–N, C–O, C=O, and O–C=O, respectively. These peaks closely matched with the original C1s spectra (Fig. 4d). Furthermore, XRD results also showed an original peak at 5.6°, corresponding to 001 planes, with an interlayer spacing of 16.97 Å. However, the intensity of the peaks was slightly reduced, which may be attributed to a minor reduction of CTAB during the washing process with methanol (Fig. 11d). Therefore, overall, the above-discussed results confirmed the excellent stability of the CGO membrane up to five cycles of dye separation/regeneration.

The long-term nanofiltration performance of the CGO-50 was further conducted to assess the stability and durability of the membrane structure at 0.5 mbar over the period. The results show in Fig. S9 the normalized permeation flux significantly decreased to 40 % from the initial flux, while maintaining a satisfactory rejection rate of up to 70 %. This reduction in flux was primarily attributed to concentration polarization [73,74]. However, as the velocity of the dye solution flowing towards the CGO membrane surface equalled the diffusion rate of the dye solution to the bulk solution caused by the concentration gradient, a boundary layer formed on the membrane surface. Subsequently, the attenuation of flux and rejection decreased gradually, yet the retention of the CGO lamellar membrane remained at 70 %.

Table 2 and Fig. 12 provide a comparison of the membrane separation performance between previously reported studies and the current work. The as-prepared CGO membrane exhibited a higher removal rate and enhanced water permeation. In summary, the overall combination of higher permeance flux, excellent rejection rates, selective separation performance, good stability, and facile regeneration of CGO membranes makes them highly promising for energy-efficient separation processes, especially in the context of rejecting negatively charged dyes.

4. Conclusion

In this work, we have successfully fabricated a positively charged surfactant cetyltrimethylammonium bromide (CTAB) intercalated graphene oxide (GO) laminated composite (CGO) membrane for nanofiltration application. The XRD results proved the interlayer spacing between CTAB and GO nanosheets was aligned with the combination of both vertical and parallel intercalation (of CTAB) and it was regulated by changing the initial concentration of CTAB. The vertically aligned CTAB play a significant role in expanding the internal layer of the CGO laminates membrane. Among the prepared membranes, the CGO-50 membranes exhibited excellent pure water flux with ~1112 L h^{-1} m^{-2} bar^{-1} with excellent separation efficiency of ~99 % for the negatively charged organic dye molecules. The electrostatic and π–π interaction mechanisms played a major role in the separation performance. In addition, the prepared CGO membrane exhibited invariable separation performance, after soaking the membrane in solutions with different pHs and DI water (with >97 % organic rejection), and water flux due to

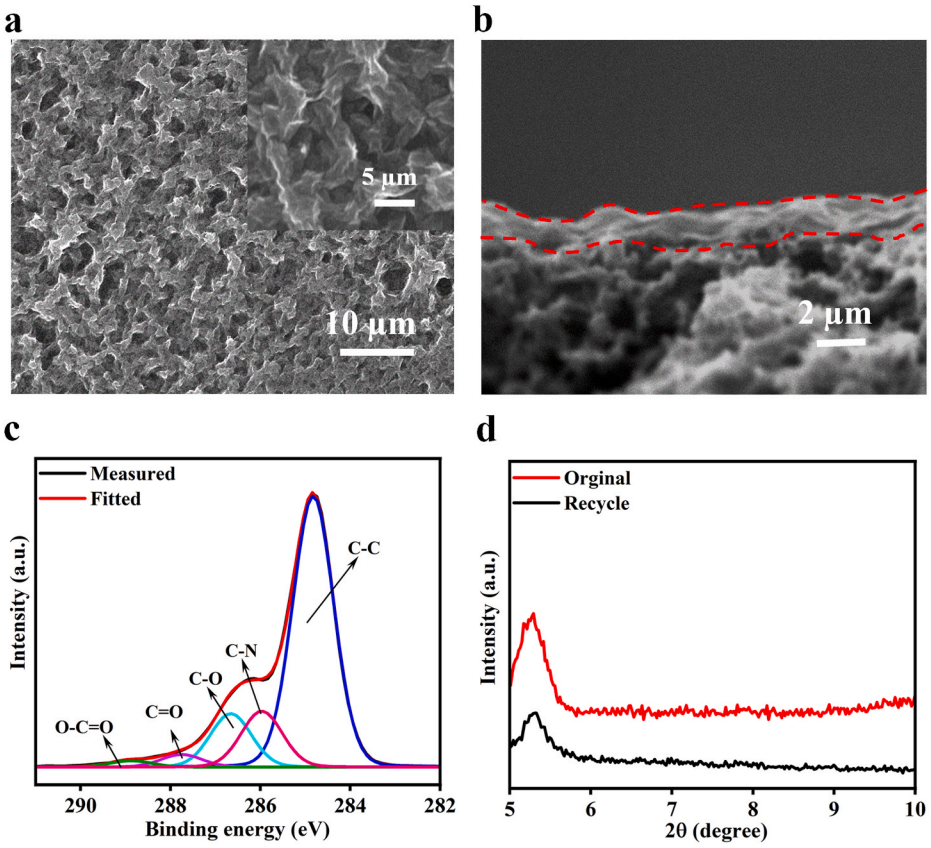


Fig. 11. Surface (a) and cross-sectional (b) SEM images, (c) XPS C1s spectra and (d) XRD spectra of the CGO membrane after five cycles of dye separation.

Table 2
Separation performance of CGO membrane and other membranes.

Membrane	Probe molecule	Water permeance (L h^{-1} m^{-2} bar^{-1})	Rejection (%)	Reference
PEI/GO@PAN	Direct red-80	117.80	99.70	[75]
TiO_2/micronized phosphate	Direct red-80	≈13.75	92.00	[76]
Nano-TiO_2	Direct red-80	≈15.00	~95.00	[77]
PSF-CS membrane	Direct red-80	160.25	99.56	[78]
PE-iGO	Direct red-80	28.30	99.65	[79]
RGO	Direct red-80	80.00	99.99	[80]
rGO	Direct red-80	21.80	99.90	[81]
GO/COF-1 membrane	Direct red-80	310.90	99.04	[82]
Ca/GO-SA3	Direct red-80	38.90	99.82	[83]
Sepro NF 6	Direct red-80	84.17	99.95	[84]
PAN-DR80 TFC	Direct red-80	~128.4	~99.90	[85]
UiO-66@GO-CS	Direct red-80	14.60	99.70	[86]
CGO	Direct red-80	~932.03	99.00	This work

its excellent chemical stability. Moreover, the permeance and rejections were recorded up to 96 % of the original performance without deterioration even after five separation cycles. In conclusion, the CGO membrane has potential application value in the separation of dye wastewater treatment in practical applications.

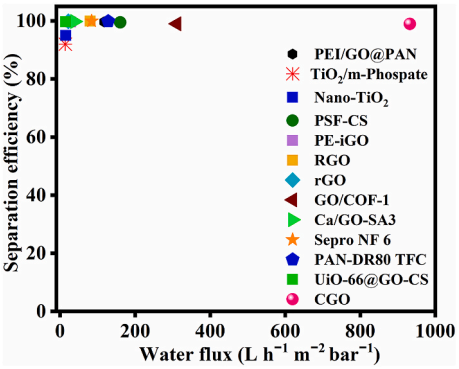


Fig. 12. Comparison of separation performance of CGO membranes prepared in this work with other reported membranes on Direct red-80. (For interpretation of the references to color in this figure legend, the reader is referred to the Web version of this article.)

Funding sources

This work was funded by Jiangsu Dingying New Materials Co., Ltd. under Grant Number [C−00005685] and the School of Engineering, the University of Edinburgh.

CRediT authorship contribution statement

Rajakumari Krishnamoorthi: Writing – review & editing, Writing – original draft, Validation, Methodology, Formal analysis, Data curation, Conceptualization. **Fraz Saeed Butt:** Writing – review & editing,

Investigation. **Nurul A. Mazlan:** Writing – review & editing, Methodology, Investigation, Formal analysis, Data curation. **Siyu Chen:** Writing – review & editing, Formal analysis, Data curation. **Norbert Radacsi:** Writing – review & editing, Resources. **Shuiqing Yang:** Writing – review & editing, Supervision. **Yeomin Yoon:** Writing – review & editing, Investigation. **Yi Huang:** Writing – review & editing, Supervision, Resources, Project administration, Methodology, Investigation, Funding acquisition, Conceptualization.

Declaration of competing interest

The authors declare that they have no known competing financial interests or personal relationships that could have appeared to influence the work reported in this paper.

Data availability

Data will be made available on request.

Acknowledgements

This work was funded by Jiangsu Dingying New Materials Co., Ltd. under Grant Number [C−00005685] and the School of Engineering, the University of Edinburgh *via* start-up funding. The authors would like to thank Fergus Dingwall for his laboratory assistance.

Appendix A. Supplementary data

Supplementary data to this article can be found online at https://doi.org/10.1016/j.memsci.2024.122942.

References

[1] O. Dubois, The State of the World's Land and Water Resources for Food and Agriculture: Managing Systems at Risk, Earthscan, 2011.
[2] X.-R. Xu, H.-B. Li, W.-H. Wang, J.-D. Gu, Decolorization of dyes and textile wastewater by potassium permanganate, Chemosphere 59 (6) (2005) 893–898, https://doi.org/10.1016/j.chemosphere.2004.11.013.
[3] S.F. Anis, B.S. Lalia, A. Lesimple, R. Hashaikeh, N.J. Hilal, Electrically conductive membranes for contemporaneous dye rejection and degradation, Chem. Eng. J. 428 (2002) 131184, https://doi.org/10.1016/j.cej.2021.131184.
[4] M. Berradi, R. Hsissou, M. Khudhair, M. Assouag, O. Cherkaoui, A. El Bachiri, A. J. El Harfi, Textile finishing dyes and their impact on aquatic environs, Heliyon 5 (11) (2019) e02711, https://doi.org/10.1016/j.heliyon.2019.e02711.
[5] X.-A. Ning, M.-Q. Lin, L.-Z. Shen, J.-H. Zhang, J.-Y. Wang, Y.-J. Wang, Z.-Y. Yang, J.-Y. Liu, Levels, composition profiles and risk assessment of polycyclic aromatic hydrocarbons (PAHs) in sludge from ten textile dyeing plants, Environ. Res. 132 (2024) 112–118, https://doi.org/10.1016/j.envres.2014.03.041.
[6] B.K. Körbahti, A. Tanyolaç, Electrochemical treatment of simulated textile wastewater with industrial components and Levafix Blue CA reactive dye: optimization through response surface methodology, J. Hazard Mater. 151 (2) (2008) 422–431, https://doi.org/10.1016/j.jhazmat.2007.06.010.
[7] X. Liang, X.A. Ning, G. Chen, M. Lin, J. Liu, Y. Wang, Concentrations and speciation of heavy metals in sludge from nine textile dyeing plants, Ecotoxicol. Environ. Saf. 98 (2013) 128–134, https://doi.org/10.1016/j.ecoenv.2013.09.012.
[8] S. Vanhulle, M. Trovaslet, E. Enaud, M. Lucas, S. Taghavi, D. Van der Lelie, B. Van Aken, M. Foret, R.C. Onderwater, D.J. Wesenberg, Decolorization, cytotoxicity, and genotoxicity reduction during a combined ozonation/fungal treatment of dye-contaminated wastewater, Environ. Sci. Technol. 42 (2) (2008) 584–589, https://doi.org/10.1021/es071300k.
[9] L. Fortunato, H. Elcik, B. Blankert, N. Ghaffour, J.J. Vrouwenvelder, Textile dye wastewater treatment by direct contact membrane distillation: membrane performance and detailed fouling analysis, J. Membr. Sci. 636 (2021) 119552, https://doi.org/10.1016/j.memsci.2021.119552.
[10] N.B. Amar, N. Kechaou, J. Palmeri, A. Deratani, A.J. Sghaier, Comparison of tertiary treatment by nanofiltration and reverse osmosis for water reuse in denim textile industry, J. Hazard Mater. 170 (1) (2009) 111–117, https://doi.org/10.1016/j.jhazmat.2009.04.130.
[11] K. Singh, S. Arora, Removal of synthetic textile dyes from wastewaters: a critical review on present treatment technologies, Crit. Rev. Environ. Sci. Technol. 41 (9) (2011) 807–878, https://doi.org/10.1080/10643380903218376.
[12] Y.J. Tan, L.J. Sun, B.T. Li, X.-H. Zhao, T. Yu, N. Ikuno, K. Ishii, H.-Y. Hu, Fouling characteristics and fouling control of reverse osmosis membranes for desalination of dyeing wastewater with high chemical oxygen demand, Desalination 419 (2017) 1–7, https://doi.org/10.1016/j.desal.2017.04.029.
[13] J. Dasgupta, J. Sikder, S. Chakraborty, S. Curcio, E. Drioli, Remediation of textile effluents by membrane-based treatment techniques: a state of the art review, J. Environ. Manag. 147 (2015) 55–72, https://doi.org/10.1016/j.jenvman.2014.08.008.
[14] S.R. Panda, S.J. De, Performance evaluation of two-stage nanofiltration for treatment of textile effluent containing reactive dyes, J. Environ. Chem. Eng. 3 (3) (2015) 1678–1690, https://doi.org/10.1016/j.jece.2015.06.004.
[15] J. Lin, W. Ye, H. Zeng, H. Yang, J. Shen, S. Darvishmanesh, P. Luis, A. Sotto, B. Van der Bruggen, Fractionation of direct dyes and salts in aqueous solution using loose nanofiltration membranes, J. Membr. Sci. 477 (2015) 183–193, https://doi.org/10.1016/j.memsci.2014.12.008.
[16] N. Hilal, H. Al-Zoubi, N. Darwish, A. Mohamma, M.A. Arabi, Comprehensive review of nanofiltration membranes: treatment, pretreatment, modelling, and atomic force microscopy, Desalination 170 (3) (2004) 281–308, https://doi.org/10.1016/j.desal.2004.01.007.
[17] S. Tul Muntha, A. Kausar, M. Siddiq, Advances in polymeric nanofiltration membrane: a review, Polym. Plast. Technol. Eng. 56 (8) (2017) 841–856, https://doi.org/10.1080/03602559.2016.1233562.
[18] J. Park, M. Oh, Construction of flexible metal–organic framework (MOF) papers through MOF growth on filter paper and their selective dye capture, Nanoscale 9 (35) (2017), https://doi.org/10.1039/C7NR04113F, 12850–1285.
[19] X. Liu, N.K. Demir, Z. Wu, K. Li, Highly water-stable zirconium metal–organic framework UiO-66 membranes supported on alumina hollow fibers for desalination, J. Am. Chem. Soc. 137 (22) (2015) 6999–7002, https://doi.org/10.1021/jacs.5b02276.
[20] T. Li, L. Liu, Z. Zhang, Z. Han, Preparation of nanofibrous metal-organic framework filter for rapid adsorption and selective separation of cationic dye from aqueous solution, Sep. Purif. Technol. 237 (2020) 116360, https://doi.org/10.1016/j.seppur.2019.116360.
[21] Q. Shi, N. Zhang, D. Wang, J. Zhang, Y. Li, Z. Wang, Polyethylenimine-mica nanosheets/cellulose nanofibers stacked loose nanofiltration membrane for effective dye/salt separation, Desalination 551 (2023) 116410, https://doi.org/10.1016/j.desal.2023.116410.
[22] M.A. Qamar, M. Javed, S. Shahid, M. Shariq, M.M. Fadhali, S.K. Ali, M. Khan, Synthesis and applications of graphitic carbon nitride (g-C3N4) based membranes for wastewater treatment: a critical review, Heliyon 9 (1) (2023) e12685, https://doi.org/10.1016/j.heliyon.2022.e12685.
[23] T.F. Ajibade, H. Tian, K.H. Lasisi, Q. Xue, W. Yao, Zhang, Multifunctional PAN UF membrane modified with 3D-MXene/O-MWCNT nanostructures for the removal of complex oil and dyes from industrial wastewater, Sep. Purif. Technol. 27 (5) (2021) 119135, https://doi.org/10.1016/j.seppur.2021.119135.
[24] S. Gu, Y. Ma, T. Zhang, Y. Yang, Li Xu, J. Li, MXene nanosheet tailored bioinspired modification of a nanofiltration membrane for dye/salt separation, ACS EST Water. 3 (7) (2023) 1756–1766, https://doi.org/10.1021/acsestwater.2c00213.
[25] A.R. Abdellah, H.N. Abdelhamid, A.-B. El-Adasy, A.A. Atalla, K.I. Aly, One-pot synthesis of hierarchical porous covalent organic frameworks and two-dimensional nanomaterials for selective removal of anionic dyes, J. Environ. Chem. Eng. 8 (5) (2020) 104054, https://doi.org/10.1016/j.jece.2020.104054.
[26] N.A. Mazlan, A. Lewis, Z. Chen, F.S. Butt, J. Han, N. Radacsi, S. Yang, Y. Huang, Photocatalytic self-cleaning graphene oxide/ZnO hybrid membrane for ultrafast cyclic small organic molecule separation, J. Membr. Sci. 697 (2024) 22539, https://doi.org/10.1016/j.memsci.2024.122539.
[27] J. Ma, D. Ping, X. Dong, Recent developments of graphene oxide-based membranes: a review, Membranes 7 (3) (2017) 52, https://doi.org/10.3390/membranes7030052.
[28] R.K. Joshi, S. Alwarappan, M. Yoshimura, V. Sahajwalla, Y. Nishina, Graphene oxide: the new membrane material, Appl. Mater. Today 1 (1) (2015) 1–12, https://doi.org/10.1016/j.apmt.2015.06.002.
[29] E.F. Januário, T.B. Vidovix, N.C. Beluci, R.M. Paixão, L. Silva, N.C. Homem, R. Bergamasco A, M.S. Vieira, Advanced graphene oxide-based membranes as a potential alternative for dyes removal: a review, Sci. Total Environ. 789 (2021) 147957, https://doi.org/10.1016/j.scitotenv.2021.147957.
[30] H. Kwon, Y. Park, E. Yang, T.H. Bae, H. T, Graphene oxide-based membranes intercalated with an aromatic crosslinker for low-pressure nanofiltration, Membranes 12 (10) (2022) 966, https://doi.org/10.3390/membranes12100966.
[31] S. Shahriari, M. Sastry, S. Panjikar, R.K. Singh Raman, Graphene and graphene oxide as a support for biomolecules in the development of biosensors, Nanotechnol. Sci. Appl. 14 (2021) 197–220, https://doi.org/10.2147/nsa.s334487.
[32] E. ang, M.-H. Ham, H.B. Park, C.-M. Kim, J.-H. Song, I.S. Kim, Tunable semi-permeability of graphene-based membranes by adjusting reduction degree of laminar graphene oxide layer, J. Membr. Sci. 547 (2018) 73–79, https://doi.org/10.1016/j.memsci.2017.10.039.
[33] K.H. Thebo, X. Qian, Q. Zhang, L. Chen, H.-M. Cheng, W. Ren, Highly stable graphene-oxide-based membranes with superior permeability, Nat. Commun. 9 (1) (2018) 1486, https://doi.org/10.1038/s41467-018-03919-0.
[34] B. Mi, Graphene oxide membranes for ionic and molecular sieving, Science 343 (6172) (2014) 740–742, https://doi.org/10.1126/science.1250247.
[35] N. Zhang, W. Qi, L. Huang, E. Jiang, J. Bao, X. Zhang, B. An, G.J. He, Review on structural control and modification of graphene oxide-based membranes in water treatment: from separation performance to robust operation, Chin. J. Chem. Eng. 27 (6) (2019) 1348–1360, https://doi.org/10.1016/j.cjche.2019.01.001.
[36] H. Jee, J. Jang, Y. Kang, T. Eisa, K.-J. Chae, I.S. Kim, E. Yang, Enhancing the dye-rejection efficiencies and stability of graphene oxide-based nanofiltration membranes via divalent cation intercalation and mild reduction, Membranes 12 (4) (2022) 402, https://doi.org/10.3390/membranes12040402.

[37] J. Zhang, S. Wan, B. Yan, L. Wang, Y. Qian, Graphene encapsulated Fe3O4 nano spindles as a superior anode material for lithium-ion batteries, J. Nanosci. Nanotechnol. 13 (6) (2013) 4364–4369, https://doi.org/10.1166/jnn.2013.7431.
[38] S. Park, K.-S. Lee, G. Bozoklu, W. Cai, S.T. Nguyen, R.S. Ruoff, Graphene oxide papers modified by divalent ions-enhancing mechanical properties via chemical cross-linking, ACS Nano 2 (3) (2008) 572–578, https://doi.org/10.1021/nn700349a.
[39] M.-M. Zhang, H.-X. Yan, C. Gong, F.-F. Zhang, Hyperbranched polysiloxane functionalization of graphene oxide for improved mechanical properties of cyanate ester nanocomposites, J. Compos. Mater. 49 (8) (2015) 939–948, https://doi.org/10.1177/0021998314527778.
[40] R.S. Zambare, X. Song, S. Bhuvana, C.Y. Tang, J.S.A. Prince, P.R. Nemade, Ionic liquid-reduced graphene oxide membrane with enhanced stability for water purification, ACS Appl. Mater. Interfaces 14 (38) (2022) 43339–43353, https://doi.org/10.1021/acsami.2c12488.
[41] S. Wang, L. Yang, G. He, B. Shi, Y. Li, H. Wu, R. Zhang, S. Nunes, Z. Jiang, Two-dimensional nanochannel membranes for molecular and ionic separations, Chem. Soc. Rev. 49 (4) (2020) 1071–1089, https://doi.org/10.1039/C9CS00751B.
[42] Y. Choi, J. Kang, E. Choi, J.Y. Kim, J.P. Kim, J.H. Kim, O. Kwon, D.W. Kim, W. D, Carbon nanotube-supported graphene oxide nanoribbon bilayer membrane for high-performance diafiltration, Chem. Eng. J. 427 (2022) 131805, https://doi.org/10.1016/j.cej.2021.131805.
[43] K. Murata, K. Mitsuoka, T. Hirai, T. Walz, P. Agre, J.B. Heymann, A. Engel, Y. Fujiyoshi, Structural determinants of water permeation through aquaporin-1, Nature 407 (6804) (2000) 599–605, https://doi.org/10.1038/35036519.
[44] G.M. Preston, T.P. Carroll, W.B. Guggino, P. Agre, Appearance of water channels in Xenopus oocytes expressing red cell CHIP28 protein, Science 256 (5055) (1992) 385–387, https://doi.org/10.1126/science.256.5055.385.
[45] M.A. Knepper, J.B. Wade, J. Terris, C.A. Ecelbarger, D. Marples, B. Mandon, C. L. Chou, B.K. Kishore, S. Nielsen, Renal aquaporins, Kidney Int. 49 (6) (1996) 1712–1717, https://doi.org/10.1038/ki.1996.253.
[46] H. Jin, F. Jiao, M.D. Daily, Y. Chen, F. Yan, Y.H. Ding, X. Zhang, E.J. Robertson, M. D. Baer, C.L. Chen, Highly stable and self-repairing membrane-mimetic 2D nanomaterials assembled from lipid-like peptoids, Nat. Commun. 7 (2016) 12252, https://doi.org/10.1038/ncomms12252.
[47] G. Goel, C. Hélix-Nielsen, H.M. Upadhyaya, S. Goel, A bibliometric study on biomimetic and bioinspired membranes for water filtration, Npj. Clean Water. 4 (1) (2021) 41, https://doi.org/10.1038/s41545-021-00131-4.
[48] J. Sahu, R.R. Karri, H.M. Zabed, S. Shams, X.J. Qi, Current perspectives and future prospects of nano-biotechnology in wastewater treatment, Separ. Purif. Rev. 50 (2) (2021) 139–158, https://doi.org/10.1080/15422119.2019.1630430.
[49] C.S. Lee, I. Kim, J.W. Jang, D. Yoon, Y.J. Lee, Aquaporin-incorporated graphene-oxide membrane for pressurized desalination with superior integrity enabled by molecular recognition, Adv. Sci. 8 (20) (2021) 2101882, https://doi.org/10.1002/advs.202101882.
[50] W. Zhang, Y. Zhang, Y. Wang, S. Tian, N. Han, W. Li, W. Wang, H. Liu, X. Yan, X. Zhang, Fluffy-like amphiphilic graphene oxide (f-GO) and its effects on improving the antifouling of PAN-based composite membranes, Desalination 527 (2022) 115575, https://doi.org/10.1016/j.desal.2022.115575.
[51] R. Li, Z. Wang, X. Gu, C. Chen, Y. Zhang, D. Hu, Study on the assembly structure variation of cetyltrimethylammonium bromide on the surface of gold nanoparticles, ACS Omega 5 (10) (2020) 4943–4952, https://doi.org/10.1021/acsomega.9b0382.
[52] K. Zhang, L. Mao, L.L. Zhang, H.S. On Chan, X.S. Zhao, J. Wu, Surfactant-intercalated, chemically reduced graphene oxide for high performance supercapacitor electrodes, J. Mater. Chem. 21 (20) (2011) 7302–7307, https://doi.org/10.1039/C1JM00007A.
[53] C.H. Chen, S. Hu, J.F. Shih, C.Y. Yang, Y.W. Luo, R.H. Jhang, C.M. Chiang, Y. J. Hung, Effective synthesis of highly oxidized graphene oxide that enables wafer-scale nanopatterning: preformed acidic oxidizing medium approach, Sci. Rep. 7 (1) (2017) 3908, https://doi.org/10.1038/s41598-017-04139-0.
[54] T. Chen, F.S. Butt, M. Zhang, X. Wei, A. Lewis, N. Radacsi, A.J. Semiao, J. Han, Y. Huang, Ultra-permeable zeolitic imidazolate frameworks-intercalated graphene oxide membranes for unprecedented ultrafast molecular separation, Chem. Eng. J. 419 (2021) 129507, https://doi.org/10.1016/j.cej.2021.129507.
[55] G. Kong, J. Pang, Y. Tang, L. Fan, H. Sun, R. Wang, S. Feng, Y. Feng, W. Fan, W. Kang, H. Guo, Z. Kang, D. Sun, Efficient dye nanofiltration of a graphene oxide membrane via combination with a covalent organic framework by hot pressing, J. Mater. Chem. A 7 (42) (2019) 24301–24310, https://doi.org/10.1039/C9TA07684K.
[56] L. Zheng, H. Li, X. Lai, W. Huang, Z. Lin, X. Zeng, Superwettable Janus nylon membrane for multifunctional emulsion separation, J. Membr. Sci. 642 (2022) 119995, https://doi.org/10.1016/j.memsci.2021.119995.
[57] M. Nasr, N. Alfryyan, S.S. Ali, H.M. Abd El-Salam, M.J. Shaban, Preparation, characterization, and performance of PES/GO woven mixed matrix nanocomposite forward osmosis membrane for water desalination, RSC Adv. 12 (39) (2022) 25654–25668, https://doi.org/10.1039/D2RA03832C.
[58] J. Wang, F. Fang, Y. Zhou, M. Yin, J. Liu, J. Wang, Y. Wu, J. Beiyuan, D. Chen D, Facile modification of graphene oxide and its application for the aqueous uranyl ion sequestration: insights on the mechanism, Chemosphere 258 (2020) 127152, https://doi.org/10.1016/j.chemosphere.2020.127152.
[59] B.-B. Feng, Z.-H. Wang, W.-H. Suo, Y. Wang, J.-C. Wen, Y.-F. Li, H.-L. Suo, M. Liu, L. Ma, Performance of graphene dispersion by using mixed surfactants, Mater. Res. Express 7 (9) (2020) 095009, https://doi.org/10.1088/2053-1591/abb2ca.
[60] Q. Liu, W. Luo, Y. Chen, H. Zou, M.J. Liang, Enhanced mechanical and thermal properties of CTAB-functionalized graphene oxide–polyphenylene sulfide composites, High Perform. Polym. 29 (8) (2017) 889–898, https://doi.org/10.1177/0954008316663810.
[61] R. Li, D. Guan, M. Wen, X. Zhang, M. Chen, H. Yang, C. Xu, Tuning interlayer spacing of graphene oxide membrane to enhance its separation performance of hydrogen isotopic water in membrane distillation, Sep. Purif. Technol. 304 (2023) 122382, https://doi.org/10.1016/j.seppur.2022.122382.
[62] X. Yang, X. Zhang, Z. Liu, Y. Ma, Y. Huang, Y. Chen, High-efficiency loading and controlled release of doxorubicin hydrochloride on graphene oxide, J. Phys. Chem. C 112 (45) (2008) 17554–17558, https://doi.org/10.1021/jp806751k.
[63] J. Su, S. He, Z. Zhao, X. Liu, H. Li, Efficient preparation of cetyltrimethylammonium bromide-graphene oxide composite and its adsorption of Congo red from aqueous solutions, Colloids Surf., A: Physicochem. Eng. 554 (2018) 227–236, https://doi.org/10.1016/j.colsurfa.2018.06.048.
[64] D. Johnson, N. Hilal, Characterization and quantification of membrane surface properties using atomic force microscopy: a comprehensive review, Desalination 356 (2015) 149–164, https://doi.org/10.1016/j.desal.2014.08.019.
[65] K. Guan, F. Liang, H. Zhu, J. Zhao, W. Jin, Incorporating graphene oxide into alginate polymer with a cationic intermediate to strengthen membrane dehydration performance, Appl. Mater. Interfaces 10 (16) (2018) 13903–13913, https://doi.org/10.1021/acsami.8b04093.
[66] W. Jang, J. Yun, K. Jeon, H. Byun, PVdF/graphene oxide hybrid membranes via electrospinning for water treatment applications, RSC Adv. 5 (58) (2015) 46711–46717, https://doi.org/10.1039/C5RA04439A.
[67] J. Lee, H.-R. Chae, Y.J. Won, K. Lee, C.-H. Lee, H.H. Lee, I.-C. Kim, J.-M. Lee, Graphene oxide nanoplatelets composite membrane with hydrophilic and antifouling properties for wastewater treatment, J. Membr. Sci. 448 (2013) 223–230, https://doi.org/10.1016/j.memsci.2013.08.017.
[68] W.L. Xu, C. Fang, F. Zhou, Z. Song, Q. Liu, R. Qiao, M. Yu, Self-assembly: a facile way of forming ultrathin, high-performance graphene oxide membranes for water purification, Nano Lett. 17 (2017) 2928–29332929, https://doi.org/10.1021/acs.nanolett.7b00148.
[69] K. Goh, W. Jiang, H.E. Karahan, S. Zhai, L. Wei, D. Yu, A.G. Fane, R. Wang, Y. J. Chen, All-carbon nanoarchitectures as high-performance separation membranes with superior stability, Adv. Funct. Mater. 25 (47) (2015) 7348–7359, https://doi.org/10.1002/adfm.201502955.
[70] Y.T. Nam, J. Choi, K.M. Kang, D.W. Kim, H.-T. Jung, Enhanced stability of laminated graphene oxide membranes for nanofiltration via interstitial amide bonding, ACS Appl. Mater. Interfaces 8 (40) (2016) 27376–27382, https://doi.org/10.1021/acsami.6b09912.
[71] H.M. Hegab, M. Ouda, P. Kallem, C. Aubry, Y. Ibrahim, F. Banat, S.W. Hasan, Ultrafast aquaporin-like multi-functionalized holey graphene membrane with tripartite nanochannels for organic solvent nanofiltration, Chem. Eng. J. 450 (2022) 138033, https://doi.org/10.1016/j.cej.2022.138033.
[72] A. Azarafza, M.A. Islam, Y. Golpazirsorkheh, I. Efteghar, M. Sadrzadeh, M. Kamkar, A.F. Shojaei, M. Younas, T.M. Aminabhavi, M. Rezakazemi, Aquaporin-based biomimetic membranes for low energy water desalination and separation applications, Adv. Funct. Mater. 33 (2023) 2213326, https://doi.org/10.1002/adfm.202213326.
[73] F. Moghadam, M. Zhai, T. Zouaoui, K. Li, Hybrid graphene oxide membranes with regulated water and ion permeation channels via functional materials, Curr. Opin. Chem. Eng. 40 (2023) 100907, https://doi.org/10.1016/j.coche.2023.100907.
[74] B. Feng, K. Xu, A. Huang, Covalent synthesis of three-dimensional graphene oxide framework (GOF) membrane for seawater desalination, Desalination 394 (2016) 123–130, https://doi.org/10.1016/j.desal.2016.04.030.
[75] C. Xing, C.Y. Liu, C. Lai, S.Q. Zhang, Tuning d-spacing of graphene oxide nanofiltration membrane for effective dye/salt separation, Rare. Met. 42 (2023) 418–429. https://doi.org/10.1007/s12598-022-02153-4.
[76] A. Bouazizi, M. Breida, A. Karim, B. Achiou, M. Ouammou, J.I. Calvo, A. Aaddane, K. Khiat, S.A. Younssi, Development of a new TiO2 ultrafiltration membrane on flat ceramic support made from natural bentonite and micronized phosphate and applied for dye removal, Ceram. Int. 43 (1) (2017) 1479–1487, https://doi.org/10.1016/j.ceramint.2016.10.118.
[77] A. Bouazizi, M. Breida, B. Achiou, M. Ouammou, J.I. Calvo, A. Aaddane, S. A. Younssi, Removal of dyes by a new nano–TiO2 ultrafiltration membrane deposited on low-cost support prepared from natural Moroccan bentonite, Appl. Clay Sci. 149 (2017) 127–135, https://doi.org/10.1016/j.clay.2017.08.019.
[78] J. Hamdan, N.S. Sabri, H. Hasbullah, M. Sokri, S.A. Rahman, F. Kadirkhan, Removal of direct red dye using polysulfone chitosan ultrafiltration membrane, Mater. Sci. Eng. 1142 (2017) 012018. https://iopscience.iop.org/article/10.1088/1757-899X/1142/1/012018.
[79] W. Ye, J. Lin, R. Borrego, D. Chen, A. Sotto, P. Luis, M. Liu, S. Zhao, C.Y. Tang, B. V. Bruggen, Advanced desalination of dye/NaCl mixtures by a loose nanofiltration membrane for digital ink-jet printing, Sep. Purif. Technol. 197 (2018) 27–35, https://doi.org/10.1016/j.seppur.2017.12.045.
[80] L. Liu, X. Xie, R.S. Zambare, A.P. Selvaraj, B.N. Sowrirajalu, X. Song, C.Y. Tang, C. Gao, Functionalized graphene oxide modified polyether sulfone membranes for low-pressure anionic dye/salt fractionation, Polymers 10 (7) (2018) 795, https://doi.org/10.3390/polym10070795.
[81] L. Huang, S. Huang, S.R. Venna, H. Lin, Rightsizing nanochannels in reduced graphene oxide membranes by solvating for dye; desalination, Environ. Sci. Technol. 52 (21) (2018) 12649–12655, https://doi.org/10.1021/acs.est.8b03661.
[82] X. Zhang, H. Li, J. Wang, D. Peng, J. Liu, Y. Zhang, In-situ grown covalent organic framework nanosheets on graphene for membrane-based dye/salt separation, J. Membr. Sci. 581 (2019) 321–330, https://doi.org/10.1016/j.memsci.2019.03.070.

[83] J. Yu, Y. Wang, Y. He, Y. Gao, R. Hou, J. Ma, L. Zhang, X. Guo, L. Chen, Calcium ion-sodium alginate double cross-linked graphene oxide nanofiltration membrane with enhanced stability for efficient separation of dyes, Sep. Purif. Technol. 276 (2021) 119348, https://doi.org/10.1016/j.seppur.2021.119348.

[84] J. Lin, W. Ye, H. Zeng, H. Yang, J. Shen, S. Darvishmanesh, P. Luis, A. Sotto, B. V. Bruggen, Fractionation of direct dyes and salts in aqueous solution using loose nanofiltration membranes, J. Membr. Sci. 477 (2015) 183–193, https://doi.org/10.1016/j.memsci.2014.12.008.

[85] L. Shen, P. Li, T. Zhang, Green and feasible fabrication of loose nanofiltration membrane with high efficiency for fractionation of dye/NaCl mixture by taking advantage of membrane fouling, J. Appl. Polym. Sci. 136 (18) (2019) 47438, https://doi.org/10.1002/app.47438.

[86] R. Chang, S. Ma, X. Guo, J. Xu, C. Zhong, R. Huang, J. Ma, Hierarchically assembled graphene oxide composite membrane with self-healing and high-efficiency water purification performance, ACS Appl. Mater. Interfaces 11 (2019) 4625–46260, https://doi.org/10.1021/acsami.9b18018.